

3D LiDAR Aided GNSS NLOS Mitigation in Urban Canyons

Weisong Wen^{ID}, Member, IEEE, and Li-Ta Hsu^{ID}, Member, IEEE

Abstract—This paper proposes a 3D LiDAR aided global navigation satellite system (GNSS) non-line-of-sight (NLOS) mitigation method due to both static buildings and dynamic objects. A sliding window map describing the environment of the ego-vehicle is first generated, based on real-time 3D point clouds from a 3D LiDAR sensor. Subsequently, the NLOS receptions are detected based on the sliding window map using a proposed quick searching method which eliminates the reliance on the initial guessing of the position of the GNSS receiver. Instead of directly excluding the detected NLOS satellites from further estimating the position, this paper rectifies the pseudo-range measurement model by (1) correcting the pseudo-range measurements if the reflecting point of the NLOS signals is detected within the sliding window map, and (2) remodeling the uncertainty in the NLOS pseudo-range measurement using a novel weighting scheme. The performance of the proposed model was experimentally evaluated in several typical urban canyons in Hong Kong using an automobile-level GNSS receiver. Furthermore, the potential of the proposed NLOS mitigation method in GNSS and the integration of inertial navigation systems were evaluated via factor graph optimization.

Index Terms—GNSS, 3D LiDAR, GNSS NLOS detection, NLOS correction and remodeling, automobile-level GNSS receiver, urban canyons.

I. INTRODUCTION

POSITIONING in urban environments [1], [2] is increasingly pertinent due to the increasing demand for autonomous driving vehicles (ADV) [3]. The global navigation satellite systems (GNSS) [4] are currently one of the principal means of providing globally-referenced positioning for the localization of ADV. The increasing availability of multiple satellite constellations enables the GNSS to provide satisfactory performance in open-sky areas [1]. However, the positioning accuracy declines significantly in highly-urbanized cities like Hong Kong, due to signal reflection caused by static buildings [5] and dynamic objects [6] like double-decker buses. The notorious non-light-of-sight (NLOS) receptions occur when the direct light-of-sight (LOS) is blocked, and the reflected signals from the same satellite are received. According to a recent review paper [7], NLOS is currently

Manuscript received 6 April 2021; revised 13 December 2021 and 15 March 2022; accepted 6 April 2022. Date of publication 25 April 2022; date of current version 11 October 2022. This work was supported by the Hong Kong Polytechnic University through the Project “Perception-Based GNSS PPP-RTK/LVINS Integrated Navigation System for Unmanned Autonomous Systems Operating in Urban Canyons” under Grant ZVZ8. The Associate Editor for this article was M. Nicoli. (*Corresponding author: Li-Ta Hsu*)

The authors are with The Department of Aeronautical and Aviation Engineering, Hong Kong Polytechnic University, Hong Kong (e-mail: lt.hsu@polyu.edu.hk).

Digital Object Identifier 10.1109/TITS.2022.3167710

the major difficulty in the use of GNSS in intelligent transportation systems. Consequently, the performance of GNSS positioning is highly influenced by real-time environmental features, such as buildings and dynamic objects. Therefore, the effective detection and understanding of the surrounding environments are crucial to improving the GNSS positioning in urban areas since GNSS positioning relies significantly on sky view visibility. The most common GNSS NLOS receptions mitigation method is the 3D mapping aided (3DMA) GNSS positioning, such as the NLOS exclusion based on 3D mapping information [8]–[10], shadow matching [11]–[13]. However, these 3DMA GNSS methods have inherent drawbacks like; 1) reliance on the availability of 3D building models and the initial guess of the GNSS receiver’s position; 2) the inability to mitigate the NLOS receptions caused by surrounding dynamic objects. The recent progress in the 3DMA GNSS positioning methods was comprehensively reviewed in our previous work [14].

Recently, 3D LiDAR sensors, the so-called “eyes” of ADV, the typical indispensable onboard sensor for autonomous driving vehicles, had been employed in the detection of NLOS caused by dynamic objects in our previous work [6]. Due to the limited field of view (FOV: $-30^\circ \sim +10^\circ$ for Velodyne HDL 32E [15]) of 3D LiDAR, only parts of a double-decker bus can be scanned. Moreover, the method [6] relies heavily on the accuracy of object detection. However, to the best of our knowledge, this is the first work that employed real-time object detection in GNSS positioning. Instead of detecting only dynamic objects, the detection of surrounding buildings using real-time 3D LiDAR point clouds [16] was explored. Due to the limited field of view of the 3D LiDAR, only parts of the buildings can be scanned. Thus information on the height of the building height was required to detect the NLOS receptions caused by the buildings. Instead of excluding the detected NLOS receptions, we explored ways in which to correct the NLOS pseudorange measurements using LiDAR. The 3D LiDAR can measure the distance from the GNSS receiver to the surface of a building that may have reflected the GNSS signal. Then the corrected and the remaining healthy GNSS measurements can both be used in further GNSS positioning. Hence, improved performance was obtained after correcting the detected NLOS satellites [16]. Unfortunately, the performance of this approach relies significantly on the accurate detection of the buildings and reflectors. The detection of the building and reflector can fail when the surface of a building is highly irregular. The limited FOV (field of view) of LiDAR remains a drawback in the detection of both dynamic and

static objects. Generally, the work reported in [6] and [16] revealed the feasibility of detecting GNSS NLOS using real-time onboard sensors; the real-time point clouds. To overcome the limited FOV of the 3D LiDAR, we explored the use of both fish-eye cameras and 3D LiDAR to detect and correct the NLOS signals [17]. The fish-eye camera was used in the detection of the NLOS signals. Meanwhile, the 3D LiDAR was employed to measure the distance between the GNSS receiver and a potential reflector causing NLOS receptions. However, this approach had similar problems with the work described in [18], [19] where the detection of the NLOS was sensitive to the illumination conditions of the environment. In summary, the 3D LiDAR aided GNSS positioning is a promising mitigation solution for the effects of NLOS receptions and has numerous advantages (1) both dynamic and static objects can be considered during the detection of NLOS (2) the detection of NLOS does not rely on an initial guess of the position of the GNSS receiver (3) the approach does not require the use of 3D building models, and the 3D LiDAR is robust against illumination conditions. However, three major drawbacks still existed (1) **Small FOV**: the limited FOV of the 3D LiDAR reduces the sensing capability (2) **Reliance on the object detection**: the detection of NLOS relies heavily on the accurate detection of the objects like double-decker buses and building, and (3) **Inefficiencies in reflector detection**: the reflector detection method described in [16] can only work when the surface of the building detected is sufficiently regular.

The recently developed LiDAR-based odometry [20], [21] enabled the registration of 3D point clouds from multiple frames into a map. Hence, the FOV of the reconstructed environment can be enhanced significantly through the accumulation of 3D point clouds from multiple frames. Inspired by this, this paper aims to alleviate the three listed disadvantages of the previously investigated 3D LiDAR aided GNSS positioning methods [6], [16], [17] through the exploitation of the potential of 3D point clouds from multiple frames. The main contributions of this paper are as follows:

(1) **Increase the FOV of 3D LiDAR for the mitigation of NLOS**: An innovative sliding window map (SWM) is generated based on real-time 3D point clouds from the 3D LiDAR. Only the 3D point clouds inside a sliding window are employed in generating the SWM since the point clouds farther away from the GNSS receiver are not necessary for the detection of the NLOS. Therefore, the magnitude of the drift of the SWM is bound to a small value. It is important to note that the SWM is generated in real-time for the detection of the GNSS NLOS. Consequently, the ability of the SWM to effectively describe the environment is significantly better than that of the 3D real-time point clouds, which leads to the subsequent enhancement of the FOV of the LiDAR sensor (*alleviate drawback 1*) which is our first contribution.

(2) **Direct GNSS NLOS identification without object detection**: since the generated SWM is in the body frame, which is located at the center of the 3D LiDAR, the orientation is directly adopted from an attitude and heading reference system (AHRS) for the transformation of the SWM from the body frame to a local (ENU) frame [22]. This differs from the previous work in [6] and [16] which required the object detection algorithm to recover the actual height of the detected

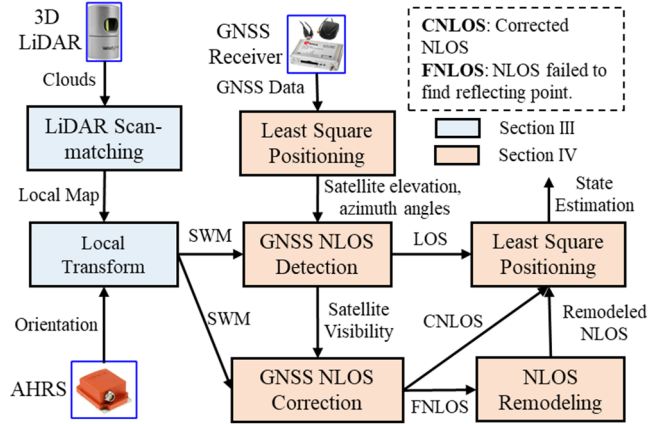


Fig. 1. Overview of the proposed method. The CNLOS denotes the detected and corrected GNSS NLOS measurements. The FNLOS denotes the detected but the reflecting point is not found in the SWM.

dynamic object or the surface of the building, both the FOV and the density of reconstructing the environment using SWM is significantly enhanced in this paper. Therefore, the NLOS receptions are directly detected based on real-time SWM, which does not require the object detection process, using a fast searching method (*relax the drawback 2*). Significantly, the proposed NLOS detection method does not rely on the initial guess of the GNSS receiver.

(3) **Direct GNSS NLOS reflector detection**: Instead of directly excluding the detected NLOS satellites from further positioning estimation, this work proposes an approach to rectify the pseudo-range measurement model by (1) correcting the pseudo-range measurements if the reflecting point of the NLOS signals is detected based on a constrained searching method (*relax the drawback 3*) inside the dense SWM and (2) re-modeling the uncertainty of NLOS pseudorange measurement using a novel weighting scheme if the reflector is not detected. This work differs from the previous work in [16] where the reflector detection algorithm requires an almost parallel distribution and the surface of the building is required to be regular, the proposed approach in this paper directly searches the potential reflectors based on the geometry captured by the SWM. Finally, both the corrected and the healthy pseudo-range measurements are used in GNSS single-point positioning (SPP).

(4) **Experimental verification**: the effectiveness of the proposed model is verified using several challenging datasets collected from the urban canyons of Hong Kong. Moreover, the feasibility of the proposed method in the integration of GNSS and inertial navigation system (INS) is also evaluated.

The subsequent sections of this paper are organized as follows; an overview of the proposed method is given in Section II. The generation of the sliding window map is elaborated in Section III. In Section IV, the proposed NLOS detection, NLOS correction, and remodeling approaches are presented. Numerous real-life experiments were performed to evaluate the effectiveness of the proposed method in Section V. Finally, Section VI presents the conclusions and the directions for future studies.

TABLE I
NOTIONS IN THIS PAPER

Notation	Description	Notation	Description
t	GNSS epoch	“G”	ECEF frame
s	Index of satellite	“L”	ENU frame
r	GNSS receiver	“BI”	AHRS body frame
ρ	Pseudorange	“BL”	LiDAR body frame
$\rho_{r,t}^s$	Pseudorange of satellite s at epoch t	“BR”	GNSS receiver body frame
$\mathbf{p}_t^{G,s}$	Position of satellite s at epoch t	$\mathbf{p}_{r,t}^G$	GNSS receiver at epoch t
$\delta_{r,t}$	Clock bias of GNSS receiver	$\delta_{r,t}^s$	Clock bias of satellite
$\psi_{r,t}^s$	Signal noise to the ratio (SNR)	K_w	Scaling factor for weightings
$\varepsilon_{r,t}^s$	Satellite elevation angle	$\alpha_{r,t}^s$	Satellite azimuth angle
k	Index of the search point	N_k	Number of neighboring points

II. SYSTEM OVERVIEW AND NOTATIONS

Fig. 1 shows an overview of the proposed method in this paper. The system consists of two parts: (1) the real-time generation of SWM based on the clouds from the 3D LiDAR and an AHRS, corresponding to the light blue shaded boxes in Fig. 1. (2) the detection and rectification of GNSS NLOS (corresponding to the light orange shaded boxes) based on the real-time description of the environment (the SWM).

In this paper, matrices are denoted with a bold uppercase letter, e.g. **G**. Vectors are denoted with bold lowercase letters, e.g. **v**. Variable scalars are with lowercase italic letters, e.g. t . Constant scalars are with lowercase letters, e.g. n. Meanwhile, the state of the GNSS receiver and the position of the satellites are all expressed in the earth-centered, earth-fixed (ECEF) frame.

It should be noted that the 3D LiDAR is only used for the description/reconstruction of the environment and the odometry of the LiDAR is not yet integrated with the GNSS which is consistent with our previous work in [16], [17]. To clearly define the proposed model, the associated notations are defined in Table I and followed by the rest of the paper. The variable expressed in the ECEF or east, north, and up (ENU) frames is denoted by superscripts “G”, “L”. For example, the transformation from the ENU to the ECEF frame is defined as $\mathbf{T}_L^G = [\mathbf{R}_L^G \mathbf{t}_L^G]$, where the \mathbf{R}_L^G and the \mathbf{t}_L^G denote the rotation and translation, respectively. The body frames of the AHRS, LiDAR, and the GNSS receiver are denoted by superscripts “BI”, “BL”, and “BR”. For example, \mathbf{P}_t^{BL} denotes a frame of 3D point clouds from the 3D LiDAR at epoch t . The orientation provided by the AHRS is denoted as $\mathbf{R}_{BI,t}^L$ at a given epoch t . The extrinsic calibration parameters between the GNSS receiver and the 3D LiDAR are denoted as \mathbf{T}_{BL}^{BR} =

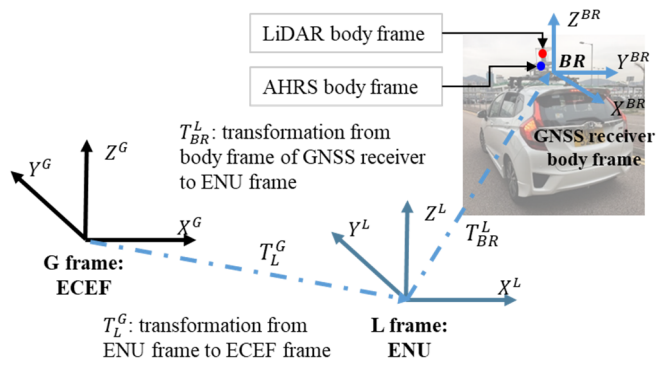


Fig. 2. Overview of the coordinate systems adopted in this paper. The ECEF frame is fixed on the center of the earth. The first point is selected as the reference of the ENU frame. The extrinsic calibration parameters between the LiDAR, AHRS, and GNSS receiver are fixed and calibrated beforehand.

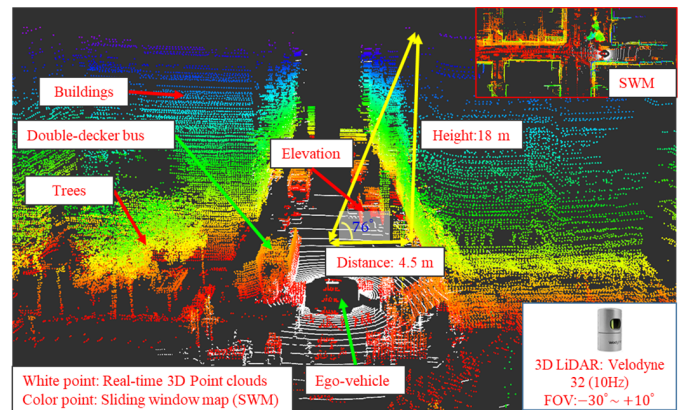


Fig. 3. Demonstration of a generated SWM and the real-time 3D point clouds. The white points represent the real-time 3D point clouds from a single frame. The colored points come from the SWM, and the color is annotated by the height information. The “distance” denotes the distance between the GNSS receiver and the building surface nearby. A video illustration of the SWM generation can be found through <https://www.youtube.com/watch?v=I6NTldUAAUM>.

[$\mathbf{R}_{BL}^{BR} \mathbf{t}_{BL}^{BR}$]. Fig. 2 illustrates the coordinate systems involved in this paper.

III. SLIDING WINDOW MAP GENERATION

This section provides a comprehensive description of the methodology involved in generating an SWM, the so-called environment description for further detection and correction of NLOS. In our previous work, described in [16], [17], [23], only real-time 3D point clouds were applied to further detect the NLOS satellites. Unfortunately, the detection capability of NLOS is limited by the FOV of the 3D LiDAR. To solve this problem, the real-time 3D point clouds are accumulated into a map that can effectively enhance the FOV of the 3D LiDAR sensor.

Fig. 3 shows the difference between the real-time 3D LiDAR point clouds and the SWM. The white points represent the 3D LiDAR. The figures revealed that only the low-lying parts of buildings or double-decker buses are scanned by the single-frame 3D point clouds (we used Velodyne 32 [15] in this paper). The visibility of

the satellite with high elevation angles cannot be effectively classified simply based on the real-time 3D point clouds. Real-time 3D point clouds are also sparse, due to the distribution of the physical scanning angle of the 3D LiDAR sensor. However, the SWM proposed in this paper can effectively ameliorate this problem. The colored points denote the mapped SWM points. Note that the ground points were removed from the SWM for efficient detection of the NLOS as described in Section IV. Fig. 3 shows that the elevation mask angle can reach 76° with the help of SWM, hence, the visibility of a satellite with an elevation angle of less than 76° can be classified in this case. The point clouds in the SWM are significantly denser than the raw real-time 3D point clouds, which can contribute significantly to the accuracy of NLOS detection. Fig. 3 shows a snapshot of the complete SWM map on the top right side. Both the buildings and the dynamic objects, such as the double-decker buses, and even the trees are involved in the SWM, which is not incorporated into the 3D building model [24].

To generate a point cloud map based on the real-time 3D point clouds, simultaneous localization and mapping (SLAM) [25] methods have been studied extensively in the past decades. Satisfactory accuracy can be obtained in a short period with low drift [26]. However, there is an accumulation of the error after long-term traveling and the loop closure is not usually available. Practically, only the objects inside a circle with a radius of about 250 meters [16] can cause GNSS NLOS receptions, and the buildings farther can be ignored. Therefore, we adopted only the last N_{sw} frames of the 3D point clouds to generate the sliding window map. Consequently, the drift error in the generation of the map is bounded at a small value and is determined by the size of the window (N_{sw}). The LiDAR odometry and mapping (LOAM) algorithm presented in [20] is a well-known method for LiDAR odometry with outperforming accuracy in the evaluated KITTI datasets. However, based on our recent evaluation in [21], the performance of the LOAM is significantly inhibited in urban canyons with numerous dynamic objects, which leads to distinct drift in the vertical direction. To fill this gap, our recent work in [21] proposed the use of the absolute ground to constrain the vertical drift, which improved the performance significantly. Therefore, we generate the SWM on top of our previous work in [21]. The detail of the SWM generation is shown in Algorithm 1.

In this case, the SWM is generated as \mathbf{M}_t^L represented in the ENU frame, which is to be used for the detection and correction of the GNSS NLOS in the next section. The size N_{sw} is set to 200 in this paper. During the implementation, we add the new LiDAR point clouds to the previously generated SWM, instead of generating the SWM using all the 3D point clouds from scratch.

IV. GNSS POSITIONING WITH PSEUDORANGE MEASUREMENT RECTIFICATION

Recently, the work in [27] described a novel general online sensor model validation and estimation framework. The framework consists of three parts: the validation, calibration, and

Algorithm 1: SWM Generation Based on 3D Point Clouds

Inputs: A series of point clouds from epoch $t - N_{sw} + 1$ to epoch t as $\{\mathbf{P}_{t-N_{sw}+1}^{BL}, \mathbf{P}_{t-N_{sw}+2}^{BL}, \dots, \mathbf{P}_t^{BL}\}$. The extrinsic parameters between the 3D LiDAR, the AHRS, and the GNSS receiver.

Outputs: The SWM \mathbf{M}_t^L

Step 1: Initialize $\mathbf{M}_t^L \leftarrow$ empty.

Step 2: SWM generation

- **Step 2-1:** Register all the point clouds $\{\mathbf{P}_{t-N_{sw}+1}^{BL}, \mathbf{P}_{t-N_{sw}+2}^{BL}, \dots, \mathbf{P}_t^{BL}\}$ into a local map (\mathbf{M}_t^{BL}) with the \mathbf{P}_t^{BL} as the first frame, based on the method in [21].

- **Step 2-2:** A point $\mathbf{M}_{t,i}^{BL}$ inside the local map \mathbf{M}_t^{BL} is transformed into the receiver body frame as $\mathbf{M}_{t,i}^{BR}$ comprising the \mathbf{M}_t^{BL}

$$\mathbf{M}_{t,i}^{BR} = \mathbf{R}_{BL}^{BR} \mathbf{M}_{t,i}^{BL} + \mathbf{t}_{BL}^{BR} \quad (1)$$

- **Step 2-3:** A point $\mathbf{M}_{t,i}^{BR}$ inside the local map \mathbf{M}_t^{BR} can be transformed into the ENU frame as $\mathbf{M}_{t,i}^L$ comprising the \mathbf{M}_t^{BL}

$$\mathbf{M}_{t,i}^L = \mathbf{R}_{BI,i}^L \mathbf{R}_{BR}^{BI} \mathbf{M}_{t,i}^{BL} + \mathbf{t}_{BR}^L \quad (2)$$

repair of the model. The authors proposed that sensor measurements should be validated, calibrated, or repaired before their integration with the data from other sensors. The main reason behind this is that sensor measurements can be affected or polluted by environmental conditions, which results in the violations of the assumptions on which the original models are built. Many sensor measurements can violate the assumptions of the standard sensor model in challenging environments like urban canyons. For example, the LiDAR-based positioning can be severely degraded in an urban canyon with numerous dynamic objects [28]. Therefore, a fixed sensor model cannot bind the potential error in the LiDAR-based positioning. Therefore, the ability to effectively validate, calibrate, and repair the sensor model as required is valuable for sensor fusion in such areas.

Following the framework proposed by Jurado and Raquet [27], we applied the three phases to the GNSS pseudo-range measurements. First, the model validation is performed based on the classification of the satellite visibility using SWM. Secondly, if one satellite is classified as NLOS, we proceed to the model calibration phase, which re-estimates the GNSS measurement by correcting the NLOS pseudo-range measurement. However, if one satellite is classified as NLOS, but its reflecting point is not found inside the SWM, which implies the unavailability of the NLOS correction, we proceed to the model repair phase by de-weighting the NLOS measurements for use in further positioning. The remainder of this section describes these three phases.

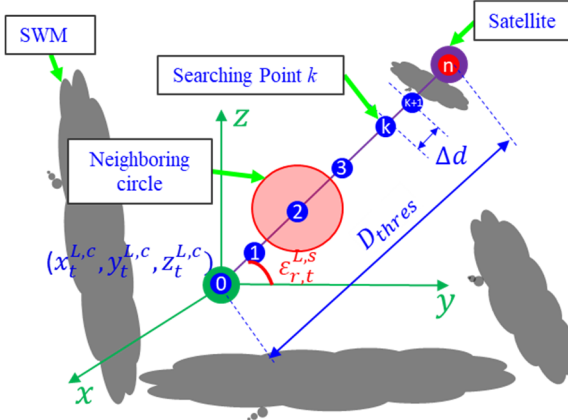


Fig. 4. Illustration of NLOS detection based on SWM.

A. Model Validation: NLOS Detection Based on SWM

In this section, we describe the details of NLOS detection based on the SWM. Unlike the 3D building models, which consist of consistent building surfaces [24], the SWM only provides unorganized discrete points. Furthermore, a fast searching method is developed for the effective classification of the satellite visibility based on the SWM (Algorithm 2).

The inputs of the algorithm include the SWM (\mathbf{M}_t^L), the elevation angle $\varepsilon_{r,t}^s$ of the satellite s , the azimuth angle $\alpha_{r,t}^s$ at epoch t , the maximum searching distance, D_{thres} , and a constant incremental value, Δd_{pix} . The output is the satellite visibility, $v_{r,t}^s$, of satellite s . In Step 1, a search point is initialized at the center of the 3D LiDAR denoted by $(x_t^{L,c}, y_t^{L,c}, z_t^{L,c})$ in the ENU frame. The superscript c denotes the center of the 3D LiDAR. A search direction connecting the GNSS receiver and the satellite is determined by the elevation and azimuth angles of satellite s . The SWM is transformed into a $kdTree$ structure [29], $\mathbf{M}_{t,tree}^L$, for the discovery of neighboring points. The $kdTree$ is a special structure for point cloud processing that can perform efficiently during the search for neighboring points. In Step 2, given a fixed incremental value, Δd_{pix} , the search point is moved to the next point $(x_{t,k}^{L,c}, y_{t,k}^{L,c}, z_{t,k}^{L,c})$ calculated using (3)-(5), based on the search direction shown on the left-hand side of Fig. 4. The k denotes the index of the search point. The number (N_k) of neighboring points close to the search point is counted. If N_k exceeds a certain threshold N_{thres} , then there are some map points from the buildings or the dynamic objects close to the search point $(x_{t,k}^{L,c}, y_{t,k}^{L,c}, z_{t,k}^{L,c})$, and we assume that the line-of-sight connecting the GNSS receiver and the satellite is blocked. Therefore, satellite s is classified as an NLOS satellite. Otherwise, Steps 2 and 3 are repeated. If $k\Delta d_{pix} > D_{thres}$, it means that the direction between the GNSS receiver and the satellite is the line-of-sight. In this work, D_{thres} was set to 250 meters, hence, points within 250 meters were considered for NLOS detection. Only the direction connecting the GNSS receiver and the satellite needs to be considered, instead of traversing the whole SWM, an approach that contributes to the efficiency of NLOS detection.

Therefore, the visibility of the satellite can be classified using Algorithm 2. Fig. 5 shows an illustration of the satellite

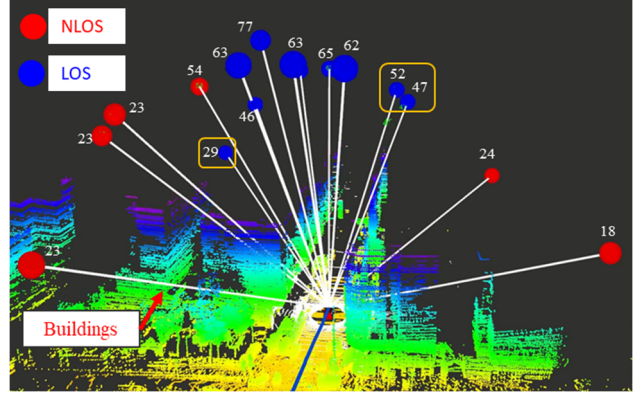


Fig. 5. Demonstration of NLOS detection based on SWM. A detailed video can be found at <https://www.youtube.com/watch?v=I6NTIdUAAM>. The circles annotated by the yellow rectangles are NLOS satellites that are not detected by the proposed method.

visibility classification result. The red and blue circles represent the NLOS and LOS satellites, respectively. The length of the line connecting the center of the 3D LiDAR and the satellite is D_{thres} . In our implementation, less than 10 ms was spent on classifying the visibility of each satellite.

The number near the circles in Fig. 5 denotes the elevation angle of the corresponding satellite. We can see that the NLOS satellite with an elevation angle of 54 degrees was detected. Fig. 3 shows that the maximum mask elevation angle can reach 76 degrees. In practice, the maximum mask elevation angle based on SWM has a significant correlation with the width of the street. The narrower the street was, the higher the mask elevation angle achieved. Although the proposed SWM effectively enhanced the FOV of the LiDAR sensor compared with our previous work described in [16], [17], [23], the SWM was still unable to fully reconstruct scenarios with very tall buildings. However, according to recent research described in [16], NLOS satellites with low elevation angles produce the majority of the GNSS positioning errors.

B. Model Calibration: NLOS Correction Based on SWM

This section presents the details of NLOS correction (model calibration) based on the SWM. To effectively estimate the potential NLOS error, the distance between the GNSS receiver, the elevation of the satellite, and the azimuth angles are needed based on the NLOS error model proposed in [30]. Therefore, the key is to detect the reflecting point corresponding to the NLOS. A ray-tracing [31] technique is commonly used to simulate the signal transmission routes of the NLOS for the discovery of the NLOS reflectors in range based on the 3DMA GNSS [5], [32]–[34]. This approach can incur a high computational load. However, unlike the 3D building models, the SWM described in this paper does not generate continuous building surfaces and clear building boundaries. The SWM only provides large amounts of dense, discrete, unorganized point clouds; there are about 10 million points inside an SWM. Instead of applying the ray-tracing technique to find the reflectors inside the SWM, we directly search for the SWM reflectors using an efficient $kdTree$ structure. The details of the

Algorithm 2: NLOS Detection Based on SWM

Inputs: Point clouds \mathbf{M}_t^L , $\varepsilon_{r,t}^s$, $\alpha_{r,t}^s$.

Outputs: Satellite visibility $v_{r,t}^{L,s}$

Step 1: Initialize the search point at $(x_t^{L,c}, y_t^{L,c}, z_t^{L,c})$, the search direction denoted by $\varepsilon_{r,t}^s$ and $\alpha_{r,t}^s$, transform the \mathbf{M}_t^L into $kdTree$ and get $\mathbf{M}_{t,tree}^L$

Step 2: Given a constant incremental value Δd_{pix} , the searching point is updated as follows:

$$x_{t,k}^{L,c} = x_{t,k-1}^{L,c} + \Delta d_{pix} \sin(\alpha_{r,t}^s) \cos(\varepsilon_{r,t}^s) \quad (3)$$

$$y_{t,k}^{L,c} = y_{t,k}^{L,c} + \Delta d_{pix} \cos(\alpha_{r,t}^s) \cos(\varepsilon_{r,t}^s) \quad (4)$$

$$z_{t,k}^{L,c} = z_{t,k-1}^{L,c} + \Delta d_{pix} \sin(\varepsilon_{r,t}^s) \quad (5)$$

Step 3: if $k \Delta d_{pix} < D_{thres}$, find the nearest neighbor points (NNPs) of a given point $(x_{t,k}^{L,c}, y_{t,k}^{L,c}, z_{t,k}^{L,c})$ and get N_k NNPs.

Step 4: Repeat Step 2~3, until $N_k > N_{thres}$. Then the satellite is NLOS ($v_{r,t}^{L,s} = 0$), else LOS ($v_{r,t}^{L,s} = 1$)

reflector detection algorithm are presented in Algorithm 3. The inputs of the algorithm include the SWM (\mathbf{M}_t^L), the elevation angle $\varepsilon_{r,t}^s$ of satellite s , the azimuth angle $\alpha_{r,t}^s$ at epoch t , and the azimuth resolution, α_{res} , as in Algorithm 2. The output is the closest reflecting point, $\mathbf{p}_{r,t}^{L,s}$, which is the most probable reflector for an NLOS satellite s .

Step1. A search point is initialized at the center of the 3D LiDAR. The search direction is determined based on the elevation of the satellite, $\varepsilon_{r,t}^s$, and the azimuth angle $\alpha_{r,t}^s$.

Step2. Two segments are included in a typical signal reflection route. The first segment is the signal transmission from the satellite to the reflector, and the second segment is the signal transmission from the reflector to the GNSS receiver. According to our previous work in [35], the reflected signal should have the same elevation angle as the expected directed signal. Therefore, all the azimuths were traversed from 0 to 360 degrees, with an azimuth resolution of α_{res} and an elevation angle of $\varepsilon_{r,t}^s$, to find all the possible NLOS transmission routes. For example, for a given direction specified by $\varepsilon_{r,t}^s$ and the azimuth angle α_s , the line-of-sight between the GNSS receiver and the satellite is identified based on Algorithm 2.

Step3. If the line-of-sight associated with the direction is blocked by a point, p_j , (Step 2 in Algorithm 3), this means that the p_j can potentially be a point of reflection. Meanwhile, if the line-of-sight connecting the point p_j and the satellite is not blocked (Step 3 in Algorithm 3), point p_j is considered a possible reflector and is saved to $\mathbf{Q}_{r,t}^{L,s}$.

Step 4. The α_s proceeds to the next azimuth based on Step 4. By replicating steps 2 and 3, all the possible reflectors are identified, based on the assumption of the same elevation angles. Fig. 6 (a)- (b) shows the result of possible reflector detection for 1-2 NLOS satellites. We observed that possible multiple reflectors are found based on Steps 1 to 4. The red circles in Fig. 6 denote the NLOS satellite, and the red lines denote possible NLOS reflection and transmission routes.

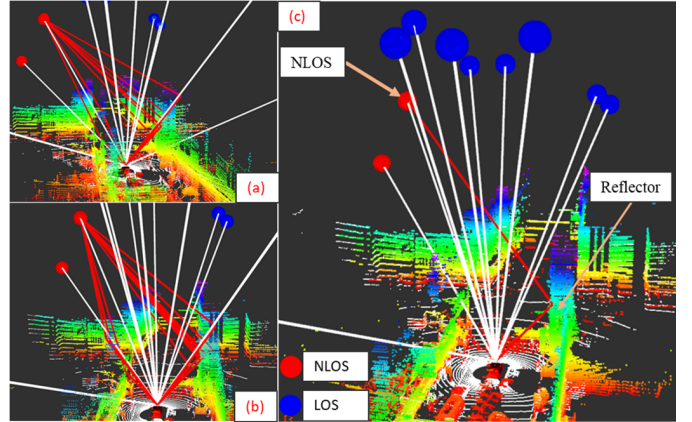


Fig. 6. Demonstration of the NLOS signal reflector detection. Red and blue circles represent NLOS and LOS satellites, respectively. White lines denote LOS transmission routes. The red lines represent NLOS transmission routes. Multiple possible NLOS transmission routes are shown in (a)-(b). The most probably NLOS transmission route is shown in (c), based on the shortest route assumption adopted in Algorithm 3.

According to [30], the reflector with the shortest distance is usually the best candidate.

Step 5. A unique reflector can be detected based on the shortest distance assumption (Step 5), as shown in Fig. 6 (c). Therefore, the reflecting point for a given satellite s is detected as $\mathbf{p}_{r,t}^{L,s}$, and the distance between the GNSS receiver can be calculated accordingly.

Algorithm 3: Reflecting Point Detection (RPD) via SWM

Inputs: Point clouds \mathbf{M}_t^L , $\varepsilon_{r,t}^s$, $\alpha_{r,t}^s$ and azimuth resolution as α_{res} .

Outputs: Reflecting point $\mathbf{p}_{r,t}^{L,s}$.

Step 1: Initialize the searching point at $(x_t^{L,c}, y_t^{L,c}, z_t^{L,c})$, the searching direction denoted by $\varepsilon_{r,t}^s$ and $\alpha_{r,t}^s$, transfer the \mathbf{M}_t^L into $kdTree$ and get $\mathbf{M}_{t,tree}^L$. Initialize reflecting points array $\mathbf{Q}_{r,t}^{L,s}$. $\alpha_s = 0$.

Step 2: Get the first point \mathbf{p}_j inside the map blocking the searching direction denoted by $\varepsilon_{r,t}^s$ and α_s using Algorithm 2. if \mathbf{p}_j is found, go to Step 3, otherwise go to Step 4.

Step 3: If the direction connecting the point and the satellite is visible, save \mathbf{p}_j to $\mathbf{Q}_{r,t}^{L,s}$, which could be a possible reflector.

Step 4: $\alpha_s \leftarrow (\alpha_s + \alpha_{res})$, repeat Steps 1 to 2 until $\alpha_s > 360^\circ$.

Step 5: find the most likely reflector \mathbf{p}_j from $\mathbf{Q}_{r,t}^{L,s}$ with the shortest distance between the GNSS receiver and the reflector. $\mathbf{p}_{r,t}^{L,s} \leftarrow \mathbf{p}_j$.

The proposed NLOS reflector detection model is not dependent on the accurate detection of the building surfaces. The short distance assumption applied in Step 5 of Algorithm 3 can effectively prevent overcorrection since only the closest reflector is identified as the unique reflector. Therefore, the reflector can be detected accordingly. Then the potential NLOS

delay for a satellite s can be calculated as $d_{r,t}^{L,s}$ [30]:

$$d_{r,t}^{L,s} = \|\mathbf{p}_{r,t}^{L,s}\| \sec(\varepsilon_{r,t}^s) + \|\mathbf{p}_{r,t}^{L,s}\| \sec(\varepsilon_{r,t}^s) \cos(2\varepsilon_{r,t}^s) \quad (6)$$

where the operator $\|\cdot\|$ is used to calculate the norm of a given vector. The $\sec(\cdot)$ denotes the secant function. Due to the sparsity of the SWM, although it is still denser than the 3D real-time point clouds, there are still some satellites whose reflectors cannot be found using the SWM. Therefore, we remodel the NLOS satellites whose reflectors are not found, using the approach described in the next section.

C. Model Repair: NLOS Remodeling

According to [30], satellites with lower elevation angles and smaller SNR have a higher chance of being contaminated by NLOS errors [30]. Modeling the uncertainty in the pseudo-range based on the elevation angle of the satellite and the SNR was reported in [36], [37]. The weighting scheme in [37] produces satisfactory performance in open areas. However, the scheme may not work in dense urban areas, since the NLOS can have high elevation angles and SNR, as shown in our previous work [17]. This weighting scheme treats the LOS and NLOS in the same manner, which is not preferable when the NLOS has already been detected. The weighting scheme in [36] employs a scaling factor to assign the LOS and NLOS different weightings. Inspired by this approach, the uncertainty in the LOS and NLOS is modeled using the weighting scheme described in [37]. A scaling factor was added to the scheme to de-weight the NLOS measurements. The selection criteria for the scaling factor can be found in [38]. Therefore, the weighting for each satellite is estimated as follows:

(1) if a satellite is classified as a LOS measurement, the weighting is calculated based on the SNR of the satellite and the angle of elevation [37].

(2) if a satellite is classified as an NLOS measurement and the pseudo-range error is corrected, the weighting is calculated based on the SNR of the satellite and the angle of elevation [37].

(3) if a satellite is classified as an NLOS measurement but the reflecting point is not detected, the weighting is calculated based on the SNR of the satellite and the angle of elevation with a scaling factor K_w [38].

D. GNSS Positioning via Weighted Least Square

The pseudo-range measurement from the GNSS receiver, $\rho_{r,t}^s$, is denoted as follows [39].

$$\rho_{r,t}^s = r_{r,t}^s + c(\delta_{r,t} - \delta_{r,t}^s) + I_{r,t}^s + T_{r,t}^s + \sigma_{r,t}^s \quad (7)$$

where $r_{r,t}^s$ is the geometric range between the satellite and the GNSS receiver. $I_{r,t}^s$ represents the ionospheric delay distance; $T_{r,t}^s$ indicates the tropospheric delay distance. $\sigma_{r,t}^s$ represents the noise resulting from the multipath effects, the NLOS receptions, the receiver noise, and the noise related to the antenna phase. Furthermore, the atmospheric effects ($T_{r,t}^s$ and $I_{r,t}^s$) are compensated for using the conventional models (Saastamoinen and Klobuchar models, respectively) presented in RTKLIB [40].

The observation model for GNSS pseudo-range measurement from a given satellite s is represented as follows:

$$\begin{aligned} \rho_{r,t}^s &= h_{r,t}^s(\mathbf{p}_{r,t}, \mathbf{p}_t^s, \delta_{r,t}) + \sigma_{r,t}^s \\ \text{with } h_{r,t}^s(\mathbf{p}_{r,t}^G, \mathbf{p}_t^{G,s}, \delta_{r,t}) &= \|\mathbf{p}_t^{G,s} - \mathbf{p}_{r,t}^G\| + \delta_{r,t} \end{aligned} \quad (8)$$

where the variable $\sigma_{r,t}^s$ stands for the noise associated with the $\rho_{r,t}^s$. It is important to note that the NLOS error $d_{r,t}^{L,s}$ is subtracted from $\rho_{r,t}^s$ before being used in further GNSS positioning. The Jacobian matrix \mathbf{G}_t^G for the observation function $h_{r,t}^s(\cdot)$ is denoted as follows:

$$\mathbf{G}_t^G = \begin{bmatrix} \frac{p_{t,x}^{G,1} - p_{\mathbf{r},t,x}^G}{\|\mathbf{p}_t^{G,1} - \mathbf{p}_{r,t}^G\|} & \frac{p_{t,y}^{G,1} - p_{\mathbf{r},t,y}^G}{\|\mathbf{p}_t^{G,1} - \mathbf{p}_{r,t}^G\|} & \frac{p_{t,z}^{G,1} - p_{\mathbf{r},t,z}^G}{\|\mathbf{p}_t^{G,1} - \mathbf{p}_{r,t}^G\|} & 1 \\ \frac{p_{t,x}^{G,2} - p_{\mathbf{r},t,x}^G}{\|\mathbf{p}_t^{G,2} - \mathbf{p}_{r,t}^G\|} & \frac{p_{t,y}^{G,2} - p_{\mathbf{r},t,y}^G}{\|\mathbf{p}_t^{G,2} - \mathbf{p}_{r,t}^G\|} & \frac{p_{t,z}^{G,2} - p_{\mathbf{r},t,z}^G}{\|\mathbf{p}_t^{G,2} - \mathbf{p}_{r,t}^G\|} & 1 \\ \frac{p_{t,x}^{G,3} - p_{\mathbf{r},t,x}^G}{\|\mathbf{p}_t^{G,3} - \mathbf{p}_{r,t}^G\|} & \frac{p_{t,y}^{G,3} - p_{\mathbf{r},t,y}^G}{\|\mathbf{p}_t^{G,3} - \mathbf{p}_{r,t}^G\|} & \frac{p_{t,z}^{G,3} - p_{\mathbf{r},t,z}^G}{\|\mathbf{p}_t^{G,3} - \mathbf{p}_{r,t}^G\|} & 1 \\ \vdots & \vdots & \vdots & \vdots \\ \frac{p_{t,x}^{G,m} - p_{\mathbf{r},t,x}^G}{\|\mathbf{p}_t^{G,m} - \mathbf{p}_{r,t}^G\|} & \frac{p_{t,y}^{G,m} - p_{\mathbf{r},t,y}^G}{\|\mathbf{p}_t^{G,m} - \mathbf{p}_{r,t}^G\|} & \frac{p_{t,z}^{G,m} - p_{\mathbf{r},t,z}^G}{\|\mathbf{p}_t^{G,m} - \mathbf{p}_{r,t}^G\|} & 1 \end{bmatrix} \quad (9)$$

where the variable m denotes the total number of satellites at epoch t . Therefore, the position of the GNSS receiver can be estimated iteratively via the least-squares as follows:

$$\begin{bmatrix} \mathbf{p}_{r,t}^G \\ \delta_{r,t} \end{bmatrix} = (\mathbf{G}_t^{G^T} \mathbf{W}_t \mathbf{G}_t^G)^{-1} \mathbf{G}_t^{G^T} \mathbf{W}_t \begin{bmatrix} \rho_{r,t}^1 \\ \vdots \\ \rho_{r,t}^m \end{bmatrix} \quad (10)$$

where the \mathbf{W}_t denotes the weighting matrix based on the estimated weights in Section IV-C as follows:

$$\mathbf{W}_t = \begin{bmatrix} \omega_{r,t}^1 & 0 & 0 & 0 \\ 0 & \omega_{r,t}^2 & 0 & 0 \\ 0 & 0 & \ddots & 0 \\ 0 & 0 & 0 & \omega_{r,t}^s \end{bmatrix}$$

$$\text{With } \omega_{r,t}^s = \begin{cases} f(\varepsilon_{r,t}^s, \psi_{r,t}^s), & \text{if LOS or CNLOS} \\ K_w f(\varepsilon_{r,t}^s, \psi_{r,t}^s), & \text{if FNLOS} \end{cases} \quad (11)$$

where the function $f(\varepsilon_{r,t}^s, \psi_{r,t}^s)$ is defined to calculate the weighting of the LOS measurements based on the SNR of the satellite and the angle of elevation as follows:

$$\begin{aligned} f(\varepsilon_{r,t}^s, \psi_{r,t}^s) &= \frac{1}{\sin^2 \varepsilon_{r,t}^s} \left(10^{-\frac{(\psi_{r,t}^s - T)}{a}} \right. \\ &\quad \times \left. \left(\left(\frac{A}{10^{-\frac{(F-T)}{a}}} - 1 \right) \frac{(\psi_{r,t}^s - T)}{F - T} + 1 \right) \right) \end{aligned} \quad (12)$$

where T indicates the SNR threshold and the parameters a , A , and F are selected based on [37].

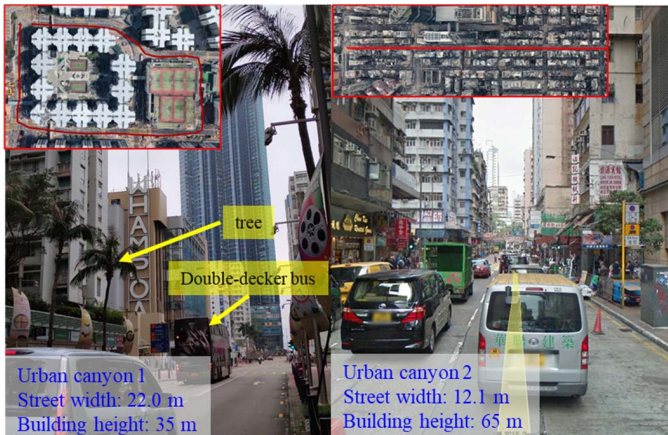


Fig. 7. Demonstration of the evaluated urban canyons 1 and 2.

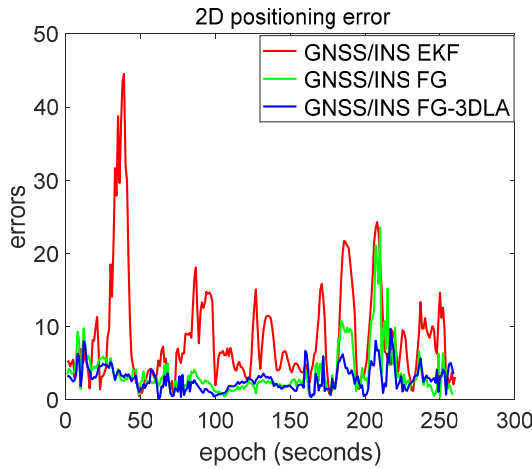


Fig. 8. 2D positioning errors of the GNSS/INS integrations in urban canyon 1.

V. EXPERIMENT RESULTS AND DISCUSSION

A. Introduction of the Experiment

1) *Experimental Scenes*: To verify the effectiveness of the proposed method, two experiments were conducted in typical urban canyons in Hong Kong (Fig. 7). The left and right figures show the evaluated urban canyons. Both urban scenarios contain static buildings, trees, and dynamic objects, like double-decker buses. We are aware of the inherent limitation of the method described in this paper, mentioned at the end of Section IV-A, that the sliding window map cannot detect the roof of buildings above 40 meters high in dense urban environments. We first experimented with a typical urban canyon in Hong Kong (urban canyon 1 in Fig. 7). Then we performed another experiment in a highly urbanized area in Hong Kong (urban canyon 2 in Fig. 7), where the buildings are significantly higher, and which is one of the densest areas in Hong Kong, to study the inherent limitations in the proposed method. Some NLOS satellites reflected by buildings taller than 40 meters may not be detected using SWM in urban canyon 2.

2) *Sensor Setups*: The detail of the data collection vehicle can be found in our open-sourced UrbanNav dataset [2].¹ In

both experiments, a u-blox M8T GNSS receiver was used for the collection of raw GNSS measurements at a frequency of 1 Hz. A 3D LiDAR sensor (Velodyne 32) was employed to collect raw 3D point clouds at a frequency of 10 Hz. The Xsens Ti-10 INS was used to collect data at a frequency of 100 Hz. Besides, the NovAtel SPAN-CPT, a GNSS (GPS, GLONASS, and Beidou) RTK/INS (fiber-optic gyroscopes, FOG) integrated navigation system was used to provide the ground truth of positioning. The gyro bias in-run stability of the FOG is 1 degree per hour, with a random walk of 0.067 degrees per hour. The baseline between the rover and the base station of the GNSS is about 7 km. All the data were collected and synchronized using a robot operation system (ROS) [41]. The coordinate systems between all the sensors were calibrated before the experiments.

3) *Evaluated Methods*: We analyzed the performance of the 3D LiDAR aided GNSS positioning through the comparison of five methods to validate the effectiveness and the reliability of the proposed method in improving the GNSS positioning as shown below:

- (a) **u-blox**: the GNSS positioning solution from the M8T u-blox receiver.
- (b) **WLS**: weighted least squares (WLS) method [37].
- (c) **WLS-NE**: weighted least squares (WLS) method [37] with the exclusion of all NLOS satellites.
- (d) **R-WLS**: WLS method with the aid of the re-weighting scheme with re-weighted NLOS satellites.
- (e) **CR-WLS**(proposed SPP): WLS method with the aid of (1) the NLOS correction proposed in Section IV-B if the reflector was detected, and (2) the re-weighting scheme in Section IV-C if the reflector was not detected.

B. Positioning Performance Evaluation

1) *GNSS Positioning in Urban Canyon 1*: Table II shows the GNSS positioning experimental results based on the five methods. The first column shows the 2D positioning error of the u-blox receiver. The positioning result is based on the standard NMEA [22] messages from the u-blox receiver. A mean error of 31.02 meters was obtained, with a standard deviation of 37.69 meters. The maximum error reached 177.59 meters due to the severe multipath and the NLOS receptions from the surrounding buildings. The GNSS solution was available throughout the experiment (100% availability). The second column shows the positioning result based on the raw pseudo-range measurements from the u-blox receiver and the positioning based on WLS. Similarly, the weighting scheme was taken from [37] and is based on the elevation angle of the satellite and the signal-to-noise ratio (SNR). The positioning error decreased to 9.57 meters with a standard deviation of 7.32 meters. The maximum error also decreased to less than 50 meters. The positioning error increased to 11.63 meters after the exclusion of all detected NLOS satellites, a result that is even worse than that of the WLS. This situation is because excessive NLOS exclusion can significantly distort the perceived geometric distribution of the satellites. Previous results [16], [17] showed a similar phenomenon. The standard deviation also increased compared with that of the WLS.

¹<https://github.com/weisongwen/UrbanNavDataset>

TABLE II

POSITIONING PERFORMANCE OF GNSS SPP IN URBAN CANYON 1 (MAX: MAXIMUM ERROR, AVAIL: AVAILABILITY OF GNSS SOLUTION)

All Data	u-blox	WLS	WLS-NE	R-WLS	CR-WLS
MEAN (m)	31.02	9.57	11.63	9.01	7.92
STD (m)	37.69	7.32	13.05	6.90	5.27
Max (m)	177.59	46.29	52.93	43.59	41.75
Avail	100 %	100%	96.01 %	100%	100%

Availability decreased slightly from 100% (WLS) to 96.01%. Therefore, complete NLOS exclusion is not suitable in dense urban canyons. The fourth column of the table presents the R-WLS results in which all the NLOS satellites were remodeled based on the weighting scheme described in Section 4.3, instead of excluding the NLOS satellites detected. The mean error of the 2D was reduced from 9.57 meters (WLS) to 9.01 meters. Both the standard deviation and the maximum errors decreased slightly. The last column shows the 2D positioning error of CR-WLS. The 2D positioning error decreased to 7.92 meters, with a standard deviation of 5.27 meters. Availability is also guaranteed using the proposed method (CR-WLS). The improved GNSS positioning results demonstrate the effectiveness of the proposed method in mitigating the effects of NLOS signals.

In summary, the optimal GNSS positioning performance was obtained using CR-WLS. These improved results showed that the proposed method can mitigate the effects of NLOS receptions by remodeling and correcting the NLOS signals. Due to the complementarity of the GNSS and the INS, it is interesting to see how the remodeling and the correction of the GNSS measurements contribute to the GNSS/INS integration which is verified in the next section.

2) *GNSS/INS Integrated Positioning in Urban Canyon 1:* This section presents the GNSS/INS integration results. In this evaluation, three GNSS/INS integrated positioning methods were also compared:

(1) **EKF:** the standard EKF-based tightly coupled GNSS/INS integration based on [42].

(2) **FG:** the factor graph-based tightly-coupled GNSS/INS integration [43].

(3) **FG-3DLA**(proposed integration): the factor graph-based tightly coupled GNSS/INS integration using 3D LiDAR aided GNSS pseudorange measurement rectification. The implementation of GNSS/INS integration using factor graph optimization (FGO) is based on our recent work in [43].

Table III shows the 2D positioning errors obtained using the three GNSS/INS integrations. A 2D mean error of 8.03 meters was obtained using the EKF procedure, with a maximum error of 44.55 meters. A significantly improved positioning accuracy was obtained after the application of the state-of-the-art FGO, with the mean error decreasing from 8.03 to 3.64 meters, with a decline in the standard deviation and the maximum error. Our recent research, described in [43], extensively evaluated the performance of GNSS/INS integration using the EKF and factor graph. Compared to conventional EKF based GNSS/INS

TABLE III

POSITIONING PERFORMANCE OF GNSS/INS INTEGRATION IN URBAN CANYON 1

GNSS/INS	EKF	FG	FG-3DLA
MEAN (m)	8.03	3.64	2.80
STD (m)	7.60	3.19	1.62
Max (m)	44.55	23.56	9.71

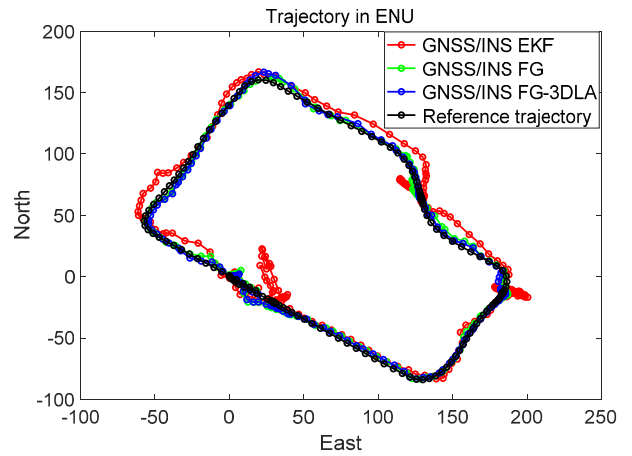


Fig. 9. 2D positioning trajectories of the GNSS/INS integrations in urban canyon 1.

integration, the FGO utilizes historical measurements during optimization, which exploits the connectivity between the historic states and the measurements. Unfortunately, the improvements from the FGO are still limited if the GNSS measurements are not adequately modeled. The maximum error still reached 23.56 meters, with a significant fluctuation in the positioning error between epochs 190 and 205 (see Fig. 8). The main reason for this variability is the high number of unmodeled NLOS measurements.

Using the proposed method, the 2D mean error decreased from 3.64 meters (FG) to 2.8 meters (FG-3DLA). The standard deviation was also reduced to 1.62 meters. The maximum 2D error was reduced from 23.56 meters (FG) to 9.71 meters. Figs. 8 and 9 show the positioning error and the trajectories, respectively. These improved results showed the effectiveness of the proposed method. Although GNSS positioning using the proposed CR-WLS still reaches 7.92 meters, the GNSS/INS integration using FGO can effectively optimize the use of the pseudo-range correction (model calibration in Section IV-B) and the uncertainty modeling (model repair in Section IV-C). After applying the 3D LiDAR aided GNSS positioning, the performance of the GNSS/INS integration using the state-of-the-art factor graph was enhanced significantly.

3) *GNSS Positioning in Urban Canyon 2:* To further verify the performance of the proposed method, another experiment was conducted in a denser urban canyon 2. As a result, the NLOS satellites with high elevation angles cannot be fully detected using the SWM. We also aimed to explore what would happen in a denser urban canyon, using the proposed method.

TABLE IV

POSITIONING PERFORMANCE OF THE GNSS SPP IN URBAN CANYON 2

All Data	u-blox	WLS	WLS-NE	R-WLS	CR-WLS
MEAN (m)	30.68	23.79	25.14	19.61	17.09
STD (m)	26.53	18.22	23.73	19.80	20.95
Max (m)	92.32	104.83	109.30	86.14	71.28
Avail	100%	100%	95.52%	100%	100%

Similar to experiment 1, the experimental GNSS positioning results are presented in Table IV to show the effectiveness of the proposed method in GNSS positioning. A positioning error of 30.68 meters was obtained using the u-blox receiver with a maximum error of 92.32 meters. A GNSS positioning error of 23.79 meters was obtained using the WLS based on the raw pseudo-range measurements from the u-blox receiver. The maximum error increased slightly to 104.83 meters, compared with the GNSS positioning using the data obtained directly from the u-blox receiver. After the exclusion of all detected NLOS satellites from the GNSS positioning (WLS-NE), both the mean and standard deviation increased to 25.14 and 23.73 meters, respectively. The availability of the GNSS positioning data decreased to 95.52%, due to the lack of satellites for GNSS positioning, which again shows that complete NLOS exclusion is not suitable in urban canyons. Based on NLOS remodeling, the 2D error decreased to 19.61 meters using R-WLS. One hundred percent availability is guaranteed. The GNSS positioning error was further decreased to 17.09 meters using the CR-WLS method. The improvement in the results shows the effectiveness of the proposed method for 3D LiDAR aided GNSS positioning. The maximum error still reached 71.28 meters since not all NLOS satellites can be detected and mitigated.

C. Discussion: Performance and the Limitation of the Proposed LOS/NLOS Detection Using SWM

1) *GNSS LOS/NLOS Detection in Urban Canyon 1:* Table V depicts the accuracy of the NLOS satellite detection. As mentioned in Section IV-A, the proposed SWM cannot fully construct all environments, hence, the inability to detect some NLOS satellites with high angles of elevation. Therefore, we evaluated the NLOS detection performance at three elevation angles. The second row in Table V shows the percentage of the NLOS satellites that belonged to a certain elevation angle range. The NLOS satellites with elevation angles between 0° and 30° accounted for 43.8% of all NLOS satellites. Among the NLOS satellites, 92% were detected using the method. The accuracy of the NLOS detection for NLOS satellites (28.9%) with elevation angles between 30° and 60° was 35%. Similar NLOS detection accuracy (27.35%) was obtained for NLOS satellites with elevation angles between 60° and 90°. Although the NLOS satellites with high elevation angles were not effectively detected, the proposed method is a novel and general solution for the

TABLE V

PERFORMANCE OF NLOS CLASSIFICATION BETWEEN DIFFERENT ELEVATION RANGES IN URBAN CANYON 1 (PER: PERCENTAGE)

All data	Elevation (0°–30°)	Elevation (30°–60°)	Elevation (60°–90°)
Per of NLOS Satellites	43.8 %	28.9%	27.35 %
Accuracy of NLOS Detection	92 %	35 %	21%

TABLE VI

PERFORMANCE OF NLOS CLASSIFICATION IN DIFFERENT ELEVATION RANGES IN URBAN CANYON 2

All data	Elevation (0°–30°)	Elevation (30°–60°)	Elevation (60°–90°)
Per of NLOS Satellites	17.7 %	38.3%	44.0 %
Accuracy of NLOS Detection (Xsens)	90.7 %	46.0%	12.0%
Accuracy of NLOS Detection (SPAN-CPT)	91.3 %	47.1%	12.5%

detection of the NLOS. Due to the decreased cost of the 3D LiDARs, the multiple 3D LiDARs [44] could be a common sensor setup for safety-critical ADV, to guarantee robustness. The use of multiple 3D LiDARs can significantly enhance the FOV of the proposed SWM. Therefore, even the NLOS satellites with high elevation angles can be detected using autonomous driving vehicles using multiple 3D LiDARs [44].

2) *GNSS LOS/NLOS Detection in Urban Canyon 2:* To further investigate the NLOS detection performance of the proposed method in urban canyon 2, we also examined the percentage of the NLOS satellites within a certain range of elevation angle in Table VI. The percentage trend is almost the complete opposite of the trend in experiment 1. The majority (44%) of the NLOS satellites belonged to the 60°–90° group in experiment 2. However, the majority of NLOS satellites belonged to the 0°–30° group in experiment 1. In experiment 2 the buildings were higher with narrower streets narrower when compared to experiment 1. The different trend is principally due to the geometry of the environments and satellite distribution. The accuracy of the NLOS detection for the satellites in the low elevation angle group (0°–30°) was still more than 90%, which is consistent with experiment 1. The NLOS detection accuracy for the satellites in the high elevation angle group (60°–90°) was limited (12%). However, the proposed method can easily be adapted to ADV with multiple 3D LiDARs to further detect NLOS satellites with high elevation angles. Since the proposed NLOS detection method is dependent on the orientation of the AHRS, we also present the effect of orientation error on the accuracy of the NLOS detection. The last row of Table VI shows the accuracy of NLOS detection at different angle ranges, using the ground truth orientation provided by the SPAN-CPT. We can see that the accuracy of the NLOS detection increased slightly.

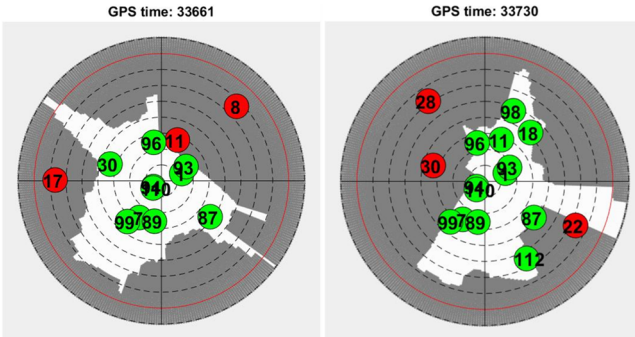


Fig. 10. Illustration of the Skyplots for epochs 33661 and 33730. The red and green circles denote the NLOS and LOS satellites, respectively. The number inside the circle represents the satellite PRN.

TABLE VII

NLOS PSEUDO-RANGE CORRECTION IN URBAN CANYON 1 AT EPOCH 33661 (PRN: PSEUDORANDOM NOISE CODE, ELE: ELEVATION ANGLE, ACTUAL: ACTUAL NLOS DELAY, ESTIMATED: NLOS DELAY ESTIMATED BY THE PROPOSED METHOD)

PRN	Ele (degree)	C/N ₀ (dB-Hz)	Actual	Estimated
8	23.49	15	15.55 m	10.08 m
17	23.13	18	13.73 m	8.14 m
11	62.45	24	3.87 m	7.59 m

TABLE VIII

NLOS PSEUDO-RANGE CORRECTION IN URBAN CANYON 1 AT EPOCH 33730

PRN	Ele (degree)	C/N ₀ (dB-Hz)	Actual	Estimated
22	26.91	19	12.02 m	10.17 m
28	28.60	18	16.41 m	9.47 m
30	56.22	30	48.52 m	27.31 m

D. Discussion: Performance and the Limitation of the Proposed NLOS Correction

1) GNSS LOS/NLOS Correction in Urban Canyon 1: Tables VII and VIII show the NLOS correction values based on the proposed method in two selected epochs. Fig. 10 shows the corresponding Skyplots. In Table VII, the NLOS satellite 8, with an elevation angle of 23.49° and C/N₀ of 15 dB-Hz, was detected and the NLOS correction was 10.08 meters. The fourth column shows the exact NLOS delay, labeled using a ray-tracing technique based on the ground truth positioning provided by the reference system SPAN-CPT. It shows that the exact NLOS delay (15.55 meters) was slightly larger than the NLOS delay estimated using the proposed method. The major reason for the difference is that the proposed method finds the reflectors based on the shortest distance assumption. Therefore, the reflector may not be perfectly detected. Generally, the results showed that the NLOS satellites with lower elevation angles usually cause larger NLOS delay, as shown in column 4 of Table VII.

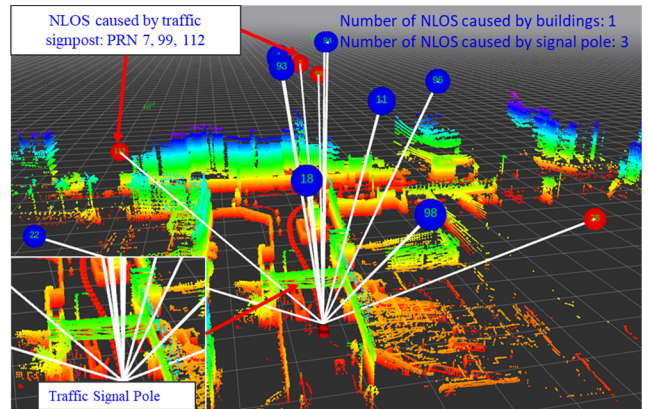


Fig. 11. Illustration of NLOS receptions blocked by an overhead traffic signal pole instead of 3D buildings. The blue and red circles denote the LOS and NLOS satellites, respectively. The numbers inside the circles denote the satellite PRN.

The epoch data shown in Table VIII shows a slightly different trend. Satellite 30, with an elevation angle of 56.22 degrees, caused the largest NLOS delay, at 48.52 meters. According to [30], the NLOS delay is determined by the elevation angle and the distance between the GNSS receiver and the reflector. The main reason for the large NLOS delay caused by satellite 30 is the long distance between the GNSS receiver and the reflector.

Fig. 11 shows a case in which the NLOS satellites were obstructed by a traffic signal pole instead of the 3D buildings. Conventionally, the 3DMA GNSS only considers static buildings. However, infrastructure such as traffic signal poles and even guard bars can also cause NLOS receptions. Satellites 7, 99, and 112 were all blocked by the signal pole. With increased complexity and density of infrastructure [45], which is not included in conventional 3D building models, the NLOS receptions caused by such structures should also be considered. We believe that this is also a significant contribution of the proposed method.

2) GNSS LOS/NLOS Correction in Urban Canyon 2: Although the mean positioning error was significantly improved compared with the 30.68 meters obtained using the u-blox, it still reached 13.32 meters. The remaining error arises from two major sources: 1) undetected NLOS satellites, and 2) unexpected multipath effects. Table VIII shows the pseudo-range errors caused by the multipath effects and the NLOS. Satellite 15 introduced the maximum pseudo-range error of 37.92 meters among the six satellites. Multipath effects can also cause errors of similar magnitude; for example, satellite 21 had a pseudo-range error of 34.88 meters. Therefore, the unmodeled multipath is a major factor behind causing the remaining 13.32 meters of positioning error. Fortunately, the multipath can further be mitigated using a higher-level GNSS antenna, which is acceptable in autonomous driving vehicles.

E. Discussion: Impacts of the Size of the SWM on the Performance of the GNSS NLOS Detection

As mentioned in Section III, the window size of the SWM is determined by N_{sw} . The too-large window size can lead to

TABLE IX
PSEUDORANGE ERRORS IN URBAN CANYON 2 (EPOCH 401793)

PRN	Ele (degree)	C/N ₀ (dB-Hz)	Type	Pseudorange Error
15	51.6	31	NLOS	37.29 m
21	48.70	26	Multipath	34.88 m
89	63.1	27	NLOS	5.71 m
92	61.63	33	Multipath	5.49 m
94	62.32	32	Multipath	5.14 m
102	60.98	34	Multipath	7.77 m

TABLE X
PERFORMANCE OF NLOS CLASSIFICATION IN DIFFERENT ELEVATION RANGES IN URBAN CANYON 2 USING DIFFERENT SIZES (N_{sw}) OF THE SWM

N_{sw}	Elevation (0°–30°)	Elevation (30°–60°)	Elevation (60°–90°)
100	50.3 %	27.0%	0.0%
150	79.3 %	35.0%	8.4%
200	90.7 %	46.0%	12.0%
250	91.2 %	46.8%	12.0%

unnecessary computation load in the GNSS NLOS detection. Conversely, a window size that is too small can not guarantee the FOV of the SWM for the GNSS NLOS detection. Hence, this paper presents the performance of the GNSS NLOS detection under different N_{sw} in Table X based on the dataset collected in urban canyon 2. It is important to note that the default value of N_{sw} is 200 in this paper.

Generally, Table X shows that the performance of the GNSS NLOS detection is improved with increased N_{sw} . Specifically, given a value of 100 for N_{sw} , only 50.3% of the GNSS NLOS receptions are detected within the elevation angles ranging from 0°–30°. Furthermore, no NLOS satellites with elevation angles ranging from 60°–90° were detected due to the small window size of the SWM. Interestingly, when the window size N_{sw} increases to 250, the improvement in GNSS NLOS detection is limited. This is because structures that are farther away may no longer cause signal blockage or reflection. However, one of the limitations of the proposed method is that the proposed method needs an initial time to accumulate the SWM before the GNSS NLOS receptions can be effectively detected. In our paper, the GNSS NLOS detection is not enabled until the N_{sw} frames of the 3D point clouds are accumulated into a reliable SWM.

VI. CONCLUSION

GNSS positioning is presently the major source of global referenced positioning for intelligent transportation systems (ITS). However, accurate GNSS positioning in urban canyons presents a major challenge due to obstructions, furthermore, NLOS receptions are currently the major problem associated with GNSS positioning in urban canyons. Therefore, effectively identifying and mitigating the effects of NLOS receptions is a significant step in enhancing the accuracy of

GNSS positioning solutions, such as SPP, real-time kinematic (RTK), and precise point positioning in urban canyons. Since the performance of GNSS positioning is heavily dependent on environmental conditions, the state-of-the-art range-based 3DMA method is proposed to effectively mitigate the NLOS effects based on offline descriptions of the environment known as the 3D building models. However, with the increasing complexity and dynamics of city infrastructures, 3D building models cannot fully describe the real-time environment. Reconstructing the real-time environment using onboard sensors is a promising method for the identification of potentially contaminated GNSS signals. Compared to the state-of-the-art 3DMA GNSS method, this paper proposes a novel 3D LiDAR aided GNSS positioning method which utilizes an onboard 3D LiDAR sensor to reconstruct the surrounding environment. Potential NLOS receptions caused by static buildings, dynamic objects, and even semi-static infrastructure (traffic signpost in Fig. 11) can be detected, remodeled, and even corrected. This paper reports a continuation of the previous work described in [16], [17], [23]. The proposed model helped in the mitigation of the three drawbacks listed in Section I, and a general solution is proposed to mitigate the effects of NLOS receptions. The method proposed in this paper can easily be adapted to the systems with multiple 3D LiDARs, and NLOS satellites with high elevation angles can be detected accordingly. Generally, we believe that the proposed method has a feasible application in academia and industry.

Since the remaining positioning error was still about 17 meters in the dense Urban Canyon 2, the LiDAR odometry should be integrated with the proposed method in subsequent works. The accuracy of the orientation could also be enhanced with the use of LiDAR odometry to further improve the NLOS detection. In addition, multiple LiDARs should be investigated to increase the FOV of the SWM generation. Therefore, it is pertinent to improve the detection and correction of GNSS NLOS with high elevation angles. Moreover, this paper only considers a single reflection from GNSS NLOS, without considering the multipath effects which are paramount inhibitors of the overall accuracy of the proposed method. In the future, we will investigate multipath mitigation using the SWM and the multiple signal reflections.

REFERENCES

- [1] S.-H. Kong, "Statistical analysis of urban GPS multipaths and pseudorange measurement errors," *IEEE Trans. Aerosp. Electron. Syst.*, vol. 47, no. 2, pp. 1101–1113, Apr. 2011.
- [2] L.-T. Hsu *et al.*, "UrbanNav: An open-sourced multisensory dataset for benchmarking positioning algorithms designed for urban areas," in *Proc. 34th Int. Tech. Meeting Satell. Division Inst. Navigat. (ION GNSS)*, Oct. 2021, pp. 226–256.
- [3] W. Wen *et al.*, "UrbanLoco: A full sensor suite dataset for mapping and localization in urban scenes," in *Proc. IEEE Int. Conf. Robot. Autom. (ICRA)*, May 2020, pp. 2310–2316.
- [4] P. K. Enge, "The global positioning system: Signals, measurements, and performance," *Int. J. Wireless Inf. Netw.*, vol. 1, no. 2, pp. 83–105, Feb. 1994.
- [5] S. Miura, L.-T. Hsu, F. Chen, and S. Kamijo, "GPS error correction with pseudorange evaluation using three-dimensional maps," *IEEE Trans. Intell. Transp. Syst.*, vol. 16, no. 6, pp. 3104–3115, Dec. 2015.
- [6] W. W. Wen, G. Zhang, and L.-T. Hsu, "GNSS NLOS exclusion based on dynamic object detection using LiDAR point cloud," *IEEE Trans. Intell. Transp. Syst.*, vol. 22, no. 2, pp. 853–862, Feb. 2021.

- [7] J. Bressler, P. Reisdorf, M. Obst, and G. Wanielik, "GNSS positioning in non-line-of-sight context—A survey," in *Proc. IEEE 19th Int. Conf. Intell. Transp. Syst. (ITSC)*, Nov. 2016, pp. 1147–1154.
- [8] C. Pinana-Diaz, R. Toledo-Moreo, D. Betaille, and A. F. Gomez-Skarmeta, "GPS multipath detection and exclusion with elevation-enhanced maps," in *Proc. 14th Int. IEEE Conf. Intell. Transp. Syst. (ITSC)*, Oct. 2011, pp. 19–24.
- [9] S. Peyraud *et al.*, "About non-line-of-sight satellite detection and exclusion in a 3D map-aided localization algorithm," *Sensors*, vol. 13, no. 1, pp. 829–847, Jan. 2013.
- [10] N. Kbayer and M. Sahmoudi, "Performances analysis of GNSS NLOS bias correction in urban environment using a three-dimensional city model and GNSS simulator," *IEEE Trans. Aerosp. Electron. Syst.*, vol. 54, no. 4, pp. 1799–1814, Aug. 2018.
- [11] P. D. Groves, L. Wang, M. Adjrad, and C. Ellul, "GNSS shadow matching: The challenges ahead," in *Proc. 28th Int. Tech. Meeting Satell. Division Inst. Navigat. (ION)*, Sep. 2015, pp. 2421–2443.
- [12] L. Wang, P. D. Groves, and M. K. Ziebart, "GNSS shadow matching: Improving urban positioning accuracy using a 3D city model with optimized visibility scoring scheme," *Navigation*, vol. 60, no. 3, pp. 195–207, 2013.
- [13] L. Wang, P. D. Groves, and M. K. Ziebart, "Smartphone shadow matching for better cross-street GNSS positioning in urban environments," *J. Navigat.*, vol. 68, no. 3, pp. 411–433, 2015.
- [14] W. Wen and L.-T. Hsu, "3D LiDAR aided GNSS and its tightly coupled integration with INS via factor graph optimization," presented at the ION GNSS, Richmond Heights, MI, USA, 2020.
- [15] F. Moosmann and C. Stiller, "Velodyne SLAM," in *Proc. IEEE Intell. Vehicles Symp. (IV)*, Jun. 2011, pp. 393–398.
- [16] W. Wen, G. Zhang, and L. Hsu, "Correcting NLOS by 3D LiDAR and building height to improve GNSS single point positioning," *Navigation*, vol. 66, no. 4, pp. 705–718, Dec. 2019.
- [17] X. Bai, W. Wen, and L. Hsu, "Using sky-pointing fish-eye camera and LiDAR to aid GNSS single-point positioning in urban canyons," *IET Intell. Transp. Syst.*, vol. 14, no. 8, pp. 908–914, Aug. 2020.
- [18] J. S. Sánchez, A. Gerhmann, P. Thevenon, P. Brocard, A. B. Afia, and O. Julien, "Use of a FishEye camera for GNSS NLOS exclusion and characterization in urban environments," in *Proc. Int. Tech. Meeting Inst. Navigat.*, Feb. 2016, pp. 283–292.
- [19] S. Kato, W. University, M. Kitamura, T. Suzuki, and Y. Amano, "NLOS satellite detection using a fish-eye camera for improving GNSS positioning accuracy in urban area," *J. Robot. Mechatronics*, vol. 28, no. 1, pp. 31–39, Feb. 2016.
- [20] J. Zhang and S. Singh, "Low-drift and real-time lidar odometry and mapping," *Auton. Robots*, vol. 41, no. 2, pp. 401–416, Feb. 2017.
- [21] W. Wen, X. Bai, and L. T. Hsu, "AGPC-SLAM: Absolute ground plane constrained 3D LiDAR SLAM," *Navigation*, 2020.
- [22] P. D. Groves, *Principles of GNSS, Inertial, and Multisensor Integrated Navigation Systems*. Norwood, MA, USA: Artech House, 2013.
- [23] W. Wen, G. Zhang, and L.-T. Hsu, "Exclusion of GNSS NLOS receptions caused by dynamic objects in heavy traffic urban scenarios using real-time 3D point cloud: An approach without 3D maps," in *Proc. IEEE/ION Position, Location Navigat. Symp. (PLANS)*, Apr. 2018, pp. 158–165.
- [24] L. T. Hsu, Y. Gu, and S. Kamijo, "NLOS correction/exclusion for GNSS measurement using RAIM and city building models," *Sensors*, vol. 15, no. 7, pp. 17329–17349, 2015.
- [25] T. Bailey and H. Durrant-Whyte, "Simultaneous localization and mapping (SLAM): Part II," *IEEE Robot. Autom. Mag.*, vol. 13, no. 3, pp. 108–117, Sep. 2006.
- [26] J. Zhang and S. Singh, "LOAM: Lidar odometry and mapping in real-time," *Robot., Sci. Syst.*, vol. 2, p. 9, Jul. 2014.
- [27] J. D. Jurado and J. F. Raquet, "Towards an online sensor model validation and estimation framework," in *Proc. IEEE/ION Position, Location Navigat. Symp. (PLANS)*, Apr. 2018, pp. 1319–1325.
- [28] W. Wen, L.-T. Hsu, and G. Zhang, "Performance analysis of NDT-based graph SLAM for autonomous vehicle in diverse typical driving scenarios of Hong Kong," *Sensors*, vol. 18, no. 11, p. 3928, Nov. 2018.
- [29] M. Greenspan and M. Yurick, "Approximate K-D tree search for efficient ICP," in *Proc. 4th Int. Conf. 3-D Digit. Imag. Modeling (DIM)*, 2003, pp. 442–448.
- [30] L.-T. Hsu, "Analysis and modeling GPS NLOS effect in highly urbanized area," *GPS Solutions*, vol. 22, no. 1, p. 7, Jan. 2018.
- [31] A. S. Glassner, *An Introduction to Ray Tracing*. Amsterdam, The Netherlands: Elsevier, 1989.
- [32] L.-T. Hsu, Y. Gu, and S. Kamijo, "3D building model-based pedestrian positioning method using GPS/GLONASS/QZSS and its reliability calculation," *GPS Solutions*, vol. 20, no. 3, pp. 413–428, 2016.
- [33] M. Obst, S. Bauer, P. Reisdorf, and G. Wanielik, "Multipath detection with 3D digital maps for robust multi-constellation GNSS/INS vehicle localization in urban areas," in *Proc. IEEE Intell. Vehicles Symp.*, Jun. 2012, pp. 184–190.
- [34] T. Suzuki and N. Kubo, "Correcting GNSS multipath errors using a 3D surface model and particle filter," in *Proc. ION GNSS*, 2013, pp. 1583–1595.
- [35] H.-F. G. N. Zhang and H. Li-Ta, "GNSS NLOS pseudorange correction based on skymask for smartphone applications," presented at the ION GNSS, Miami, FL, USA, 2019.
- [36] S. Tay and J. Marais, "Weighting models for GPS Pseudorange observations for land transportation in urban canyons," in *Proc. 6th Eur. Workshop GNSS Signals Signal Process.*, 2013, p. 4p.
- [37] A. M. Herrera, H. F. Suhandri, E. Realini, M. Reguzzoni, and M. C. de Lacy, "goGPS: Open-source MATLAB software," *GPS Solutions*, vol. 20, no. 3, pp. 595–603, 2016.
- [38] W. Wen, X. Bai, Y. C. Kan, and L.-T. Hsu, "Tightly coupled GNSS/INS integration via factor graph and aided by fish-eye camera," *IEEE Trans. Veh. Technol.*, vol. 68, no. 11, pp. 10651–10662, Nov. 2019.
- [39] E. Kaplan and C. Hegarty, *Understanding GPS: Principles and Applications*. Norwood, MA, USA: Artech House, 2005.
- [40] T. Takasu and A. Yasuda, "Development of the low-cost RTK-GPS receiver with an open source program package RTKLlib," in *Proc. Int. Symp. GPS/GNSS*, 2009, pp. 4–6.
- [41] M. Quigley *et al.*, "ROS: An open-source robot operating system," in *Proc. Workshop Open Source Softw. (ICRA)*, 2009, vol. 3, no. 3, p. 5.
- [42] G. Falco, G. Marucco, and M. Pini, "Loose and tight GNSS/INS integrations: Comparison of performance assessed in real urban scenarios," *Sensors*, vol. 17, no. 255, p. 255, Jan. 2017.
- [43] W. Wen, T. Pfeifer, X. Bai, and L. T. Hsu, "Factor graph optimization for GNSS/INS integration: A comparison with the extended Kalman filter," *J. Inst. Navigat.*, vol. 68, no. 2, pp. 315–331, 2020.
- [44] J. Jiao, Y. Yu, Q. Liao, H. Ye, and M. Liu, "Automatic calibration of multiple 3D LiDARs in urban environments," 2019, *arXiv:1905.04912*.
- [45] C. M. Silva, B. M. Masini, G. Ferrari, and I. Thibault, "A survey on infrastructure-based vehicular networks," *Mobile Inf. Syst.*, vol. 2017, pp. 1–28, Aug. 2017.



Weisong Wen (Member, IEEE) was born in Ganzhou, Jiangxi, China. He received the Ph.D. degree in mechanical engineering, The Hong Kong Polytechnic University. He was a Visiting Student Researcher at the University of California, Berkeley (UCB) in 2018. He is currently a Research Assistant Professor with the Department of Aeronautical and Aviation Engineering, Hong Kong Polytechnic University. His research interests include multi-sensor integrated localization for autonomous vehicles, SLAM, and GNSS positioning in urban canyons.



Li-Ta Hsu (Member, IEEE) received the B.S. and Ph.D. degrees in aeronautics and astronautics from the National Cheng Kung University, Taiwan, in 2007 and 2013, respectively. In 2012, he was a Visiting Scholar at University College London, U.K. He is currently an Associate Professor with the Department of Aeronautical and Aviation Engineering, The Hong Kong Polytechnic University, before he was a Post-Doctoral Researcher with the Institute of Industrial Science, The University of Tokyo, Japan. His research interests include GNSS positioning in challenging environments and localization for pedestrian, autonomous driving vehicle, and unmanned aerial vehicle.